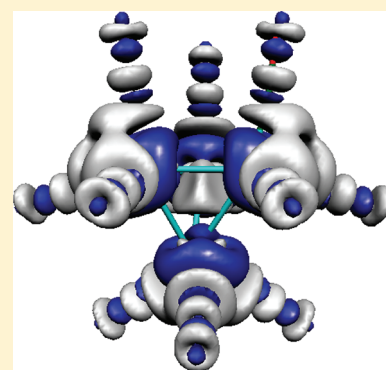


# Coverage-Dependent Adsorption Energy of Carbon Monoxide on a Rhodium Nanocluster

Constantinos D. Zeinalipour-Yazdi<sup>\*,†</sup> and Rutger A. van Santen<sup>‡</sup><sup>†</sup>CySilicoTech Research Limited, 64 Kronou Street, 2048 Nicosia, Cyprus<sup>‡</sup>Schuit Institute of Catalysis, Eindhoven University of Technology, P.O. Box 513, 5600 MB Eindhoven, Netherland**S** Supporting Information

**ABSTRACT:** Metal–adsorbate nanoclusters serve as useful models to study elementary catalytic and gas-sensor processes. However, little is known about their structural, energetic, and spectroscopic properties as a function of adsorbate surface coverage and structure. Here, we perform a systematic study of the adsorption of carbon monoxide (CO) on a tetra-atomic rhodium cluster to understand the coverage- and structure-dependent adsorption energy of CO as a function of CO coverage and to provide deeper insight into the metacarbonyl bond on metal nanoclusters. The coverage-dependent adsorption energy trends are rationalized with a use of a theoretical model, molecular orbital energy diagrams, electron density difference plots, molecular electrostatic potential plots, and simulated infrared spectra. Our model demonstrates that a critical parameter that determines the coverage-dependent energetics of the adsorption of CO at low coverages is the polarization of metal–metal  $\pi$ -bonds during the effective charge transfer, occurring from the metal cluster to the  $2\pi^*_{2p_y}$  and  $2\pi^*_{2p_x}$  states of CO, which



enhances the adsorption of CO vertical to the metal–metal bond. This configuration specific effect explains the negative coverage-dependent adsorption energy trend observed at low coverages on metal nanoclusters.

**■ INTRODUCTION**

Carbon monoxide (CO) has been considered as a probe molecule to study the adsorption of close-shell molecules on metal surfaces from both the experimental<sup>1,2</sup> and theoretical<sup>3</sup> point of view, for more than 30 years. The ground-state ( $^1\Sigma^+$ ) electronic configuration of CO can be written as,  $(1\sigma)^2(2\sigma)^2(3\sigma)^2(4\sigma)^2(1\pi)^4(5\sigma)^2$ , in terms of a single configuration (Figure 1).

The  $1\sigma_{1s}$  and  $2\sigma^*_{1s}$  molecular orbitals (MOs) are primarily the  $1s$  orbitals of oxygen and carbon, respectively, which are core orbitals, and therefore, cannot participate in chemical bonding interactions. These MOs, which are centered at the carbon and oxygen nuclei are not expected to take part, or to be affected by the formation of the metacarbonyl (M–CO) bond as their overlap with adjacent orbitals is limited by their relatively small radial size. In contrast, the spatially more extended bonding  $3\sigma_{2s}$  and antibonding  $4\sigma^*_{2s}$  MOs, which are formed due to in-phase and out-of-phase overlap of the  $2s$  atomic orbitals, cause the formation of *one*  $\sigma$ -bond between C and O. There are also *two*  $\pi$ -bonds that are formed due to the parallel overlap of the  $2p_y$  and  $2p_x$  atomic orbitals. The  $\sigma$ -bond is generally not important for the formation of the M–CO bond but may be affected by it, due to Pauli repulsion, by the increase of electron density in the doubly degenerate  $1\pi$  MOs ( $1\pi_{2p_y}$ ,  $1\pi_{2p_x}$ ), as a result of increase in antibonding character of the doubly degenerate  $2\pi^*$  MOs ( $2\pi^*_{2p_y}$ ,  $2\pi^*_{2p_x}$ ). This interpretation, based on the pioneering studies of Blyholder,<sup>3</sup> Bagus et al.,<sup>4,5</sup> and Hoffman et al.<sup>6</sup> is due to  $\pi$ -back-donation

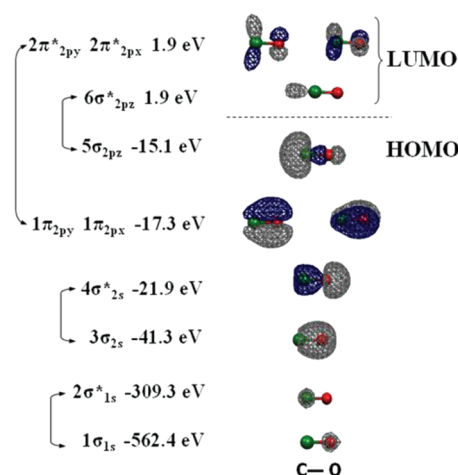


**Figure 1.** Electronic structure energy diagram and molecular orbitals of CO calculated at the CCSD(T)/aug-cc-pVTZ(5d,7f) level of theory.

from filled metal  $d$  states to the unoccupied  $2\pi^*$  MOs of CO. Another driving force for the formation of the M–CO bond is the interaction of the highest occupied molecular orbital (HOMO) denoted as  $5\sigma_{2p_z}$  with empty  $d$ -orbitals at the metal.

Received: September 17, 2011

Revised: April 1, 2012

Published: April 1, 2012

This interaction, usually referred to as  $\sigma$ -donation, was initially described by Blyholder<sup>3</sup> but was later challenged by the theoretical studies of Bagus et al.<sup>4,5</sup> and Hoffman et al.<sup>6</sup> that showed that the interaction of HOMO orbital of CO with the metal is actually *repulsive*, an issue that was also experimentally addressed by X-ray emission spectroscopy (XES) studies.<sup>7–9</sup> Although these first studies were based on cluster/adsorbate systems, a widely used model derived for extended metal surfaces, the *d-band model*, was later derived by Hammers et al.<sup>10</sup> This model showed that a key parameter for late transition metals during the formation of the metal–CO bond is the effective charge transfer from the metal to the empty  $2\pi^*$  states of CO. Recently, Zeinalipour et al.<sup>11</sup> has demonstrated through spin-unrestricted density functional theory (DFT) calculations that the C–O vibrational frequency on dimeric and tetrameric transition and noble metal clusters (i.e.,  $d^6$ ,  $d^7$ ,  $d^8$ , and  $d^9$  electronic configurations) is better described by  $\pi$ -back-donation and  $\sigma$ -repulsion as it increases as a function of the principal quantum number ( $n$ ) and the number of d electrons of the valence shell of the metal.

Apart from the fundamental interest in obtaining a deeper understanding of the electronic structure of the rhodium–CO bond on clusters, there are various applied fields in which such studies generate valuable fundamental and practical insight. For example, cluster/adsorbate model systems can act as useful models to predict trends that are also valid for the substrate/metal system and this way direct research toward the finding of novel properties to improve the operation of fuel cells<sup>12</sup> and CO trace-gas sensors.<sup>13</sup> Additionally, these type of studies provide insight in elementary catalytic processes as CO adsorption is also one of the important chemical steps in many industrial processes (i.e., three-way catalytic (TWC) converter,<sup>14</sup> water–gas shift<sup>15,16</sup> (WGS) process, Fischer–Tropsch<sup>17</sup> (F–T) reaction). The common issue in all aforementioned processes is that CO may adsorb too strongly on the metal (i.e., clusters, nanoparticles, surfaces) leading to the irreversible binding and hence, poisoning, deactivation, and/or degradation of catalysts.<sup>18</sup> For example, the platinum (Pt) electrodes in proton-exchange-membrane fuel cells<sup>19</sup> (PEMFC) are deactivated by low CO concentrations in the reactant feedstream (<5 ppm). Likewise, strong CO adsorption deactivates or even degrades the active material in CO gas sensors.<sup>20</sup> Therefore, elevated temperatures are required to establish a reversible adsorption of CO, which in catalysis causes sintering of catalysts and higher operational costs. For other applications such conditions may fall outside the operational temperature range of the device. In most cases materials that adsorb CO weakly are desirable and because it is generally known that the chemisorption energy of adsorbates can considerably be affected by their surface coverage, it is useful to understand the coverage-dependent adsorption energy of CO to small clusters, as model systems. Experimentally, this has been a well addressed topic for extended surfaces as there are numerous studies of the adsorption of CO using infrared spectroscopy and temperature-programmed desorption (TPD) studies. These studies have reached the consensus that a weakening of the M–CO bond occurs as a function of the surface coverage of CO ( $\theta_{CO}$ ) and an enhancement of the C–O bond strength, which consequently leads to the blue shift of the carbonyl infrared absorption band. Therefore, infrared spectroscopy has been broadly used as a suitable technique to study the adsorption of CO to metals due to the sensitivity of the

carbonyl vibrational frequency to the M–CO adsorption energy and structure.<sup>21,22</sup>

There are numerous first-principle studies that explore the adsorption of CO on various extended surfaces (i.e., flat,<sup>6,23–26</sup> stepped,<sup>27–29</sup> kinked<sup>28</sup>) and neutral, anionic, and cationic clusters,<sup>30–35</sup> of transition and noble metals. Other phenomena, such as the diffusion<sup>36</sup> of CO on surfaces, adsorption induced surface reconstruction,<sup>18</sup> and the decomposition/activation<sup>37–41</sup> of CO that are closely related to the adsorption energy of CO have also been studied as well as the adsorption of CO to bimetallic alloys.<sup>42–45</sup> However, there are only a few first-principle studies that explore the coverage-dependent adsorption of CO on metallic surfaces.<sup>25,41,46,47</sup> Apart from a recent study by Schaefer et al.,<sup>48</sup> on binuclear homoleptic rhodium carbonyls, to the best of the authors' knowledge, there is an absence of a study that explores the coverage-dependent adsorption free energy of CO to a tetratomic metal nanocluster. In this paper, we performed calculations on a series of models, where CO was gradually adsorbed to perform an in-depth investigation of the coverage-dependent adsorption and infrared characteristics of CO adsorbed to a tetrahedral rhodium nanocluster,  $Rh_4(3,1)$  (trigonal pyramidal geometry). Our systematic study yields certain useful trends with respect to the structural, energetic and spectroscopic perturbations that occur during the adsorption of CO to  $Rh_4(3,1)$  and a simple model is derived that reproduces the calculated DFT data.

The rest of the paper has the following structure: First, a series of metal carbonyl complexes are presented for which the adsorption-induced perturbations are analyzed. Then, the coverage-dependent adsorption trends are analyzed and explained through a semiquantitative model. Then, we explore through infrared absorption spectra simulations the coverage-dependent infrared absorption characteristics of the model system under study. Finally, we present electron density difference and electrostatic potential plots that provide deeper insight into the metal–carbonyl bond on rhodium nanoclusters.

## ■ THEORETICAL CALCULATIONS

Unrestricted density functional theory (DFT) computations are employed, as implemented in NWChem<sup>49</sup> and Gaussian 03,<sup>50</sup> with the use of Becke's three-parameter hybrid exchange functional<sup>51</sup> (XC) combined with the Lee–Yang–Parr nonlocal correlation functional,<sup>52</sup> abbreviated as UB3LYP. Initially, an extended basis set saturation test was performed using the Stevens/Basch/Krauss effective core potential (ECP) triple-split basis, denoted as CEP-121G<sup>53–55</sup> and the correlation consistent augmented valence triple- $\zeta$  basis sets of the type aug-cc-pVXZ,<sup>56–60</sup> where X = D, T, Q with and without basis set superposition error (BSSE) corrections,<sup>61</sup> to establish the quality of our computational setup. Linear dependencies of the basis functions were removed by using the spherical version (Sd, 7f) of these basis sets. Eventually, all computations were performed using the UB3LYP/CEP-121G(Rh),aug-cc-pVTZ-(C,O) method (unless otherwise noted) as the BSSE-corrected adsorption energies using the aug-cc-VQZ basis set differed by only 2 kJ/mol from the non-BSSE corrected adsorption energies using the aug-cc-pVTZ basis set. This model/method served as a good compromise between computational accuracy and demand. The Hessian was calculated analytically at every optimization step, and all structures were confirmed to possess energetic minima on the potential energy surface by the absence of negative vibrational frequencies. Convergence was generally achieved by first optimizing the complex with a frozen

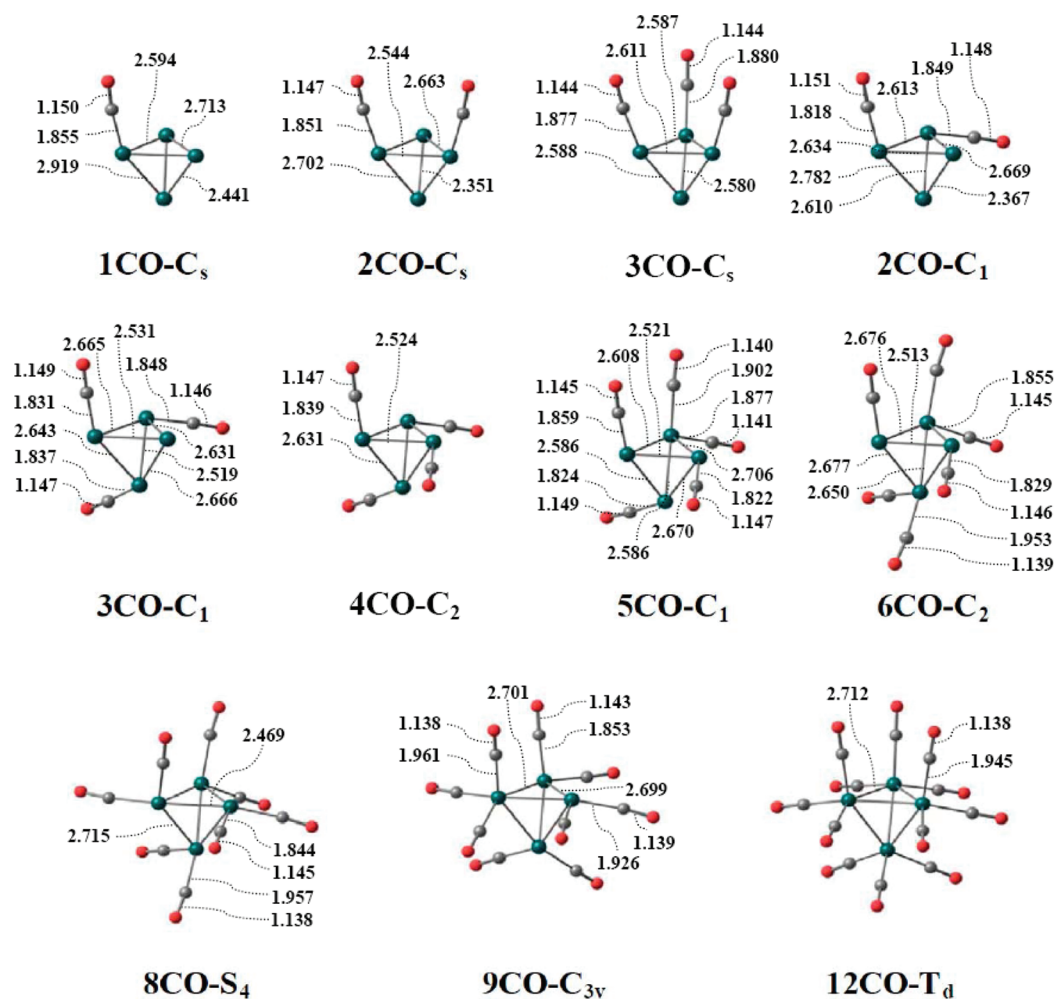


**Figure 2.** Three-dimensional structures of fully optimized rhodium carbonyl clusters of the form  $\text{Rh}_4(3,1)(\text{CO})_n$ , where  $n = 1-9$  and 12 in their lowest energy spin state. All symmetry unique bond lengths and molecular point group symmetries of the fully optimized structures at B3LYP/CEP-121G(Rh),aug-cc-pVTZ(C,O) are presented. The rhodium, carbon, and oxygen atoms are shown in black, white, and dark gray, respectively. Bond lengths are reported in Angstroms. The average bond length of the bare cluster was 2.578 Å. Cartesian coordinates of all the structures are given in the Supporting Information S-Table 1.

metal core and subsequently performing a full optimization of the cluster-adsorbate system. We note that this approach was found to be critical to achieve convergence and to significantly reduce the computational time required. The SCF convergence criteria for the root-mean-square (rms) density matrix and the total energy were set to  $10^{-8}$  Hartrees/bohr and  $10^{-6}$  Hartrees, respectively. All computations were checked for spin-contamination, which was found to be negligible and only structures with linearly adsorbed CO are reported. The equations used to derive Gibbs free energies from DFT-derived total energies are described in ref 62. The free energy of adsorption per CO ( $\Delta G_{\text{CO}}^{\circ}$ ) was calculated using

$$\Delta G_{\text{CO}}^{\circ} = (G_{\text{Rh}_4(\text{CO})_n}^{\circ} - G_{\text{Rh}_4}^{\circ} - n \cdot G_{\text{CO}}^{\circ}) / n \quad (1)$$

where  $G_{\text{Rh}_4(\text{CO})_n}^{\circ}$ ,  $G_{\text{Rh}_4}^{\circ}$ , and  $G_{\text{CO}}^{\circ}$  are the Gibbs free energies of the rhodium carbonyl complex, of the rhodium cluster, and gas phase CO, respectively,  $^{\circ}$  represents standard ambient temperature and pressure conditions (SATP,  $P = 1$  bar,  $T = 298.15$  K), and  $n$  is the number of CO molecules bound to the cluster. The cluster coverage ( $\theta_{\text{CO}}$ ) was defined on the basis of the molecular formula of tetrarhodium dodecarbonyl<sup>63</sup>  $\text{Rh}_4(\text{CO})_{12}$  using the relationship,

$$\theta_{\text{CO}} = n/12 \quad (2)$$

The IR spectra were simulated in a devoted program written in Python by fitting Lorentzian functions<sup>16</sup> of the form

$$L(\tilde{\nu}) = \sum_i \frac{f_i}{\pi} \frac{\frac{1}{2}\Gamma_{1/2}}{(\tilde{\nu} - \tilde{\nu}_i)^2 + \left(\frac{1}{2}\Gamma_{1/2}\right)^2} \quad (3)$$

where  $f_i$  and  $\tilde{\nu}_i$  are the oscillator strengths and frequencies ( $\text{cm}^{-1}$ ) of the various vibrational modes and  $\Gamma_{1/2}$  the full-width-at-half-maximum for each Lorentzian, set to  $15 \text{ cm}^{-1}$ .<sup>64</sup> The total integrated intensity of the adsorption spectrum ( $0-4000 \text{ cm}^{-1}$ ) was set equal to the sum of the oscillator strength using the following relationship,

$$\int_{4000}^0 L(\tilde{\nu}) d\tilde{\nu} = \sum_i f_i \quad (4)$$

## RESULTS AND DISCUSSION

**Optimized Cluster Adsorbate Structures.** To examine the coverage-dependent adsorption energy of CO on  $\text{Rh}_4(3,1)$ , we first designed a series of rhodium-carbonyl clusters with the

**Table 1. Free Energies ( $G^\circ$ ) of the Rhodium Carbonyl Clusters of the Form  $\text{Rh}_4(3,1)(\text{CO})_n$ , where  $n = 1-9$  and 12 Obtained at B3LYP/CEP-121G(Rh),aug-cc-pvTZ(C,O) and for Spin Multiplicities (SM) of 1, 3, 5, 7, and 9<sup>a</sup>**

molecular formula <sup>b</sup>	point group symmetry	label	$\theta_{\text{CO}}^c$	$G^\circ(\text{SM}=1)$ (kJ/mol)	$G^\circ(\text{SM}=3)$ (kJ/mol)	$G^\circ(\text{SM}=5)$ (kJ/mol)	$G^\circ(\text{SM}=7)$ (kJ/mol)	$G^\circ(\text{SM}=9)$ (kJ/mol)	DFT $\Delta G_{\text{CO}}^\circ$ (kJ/mol)	model $\Delta G_{\text{CO}}^\circ$ (kJ/mol)
$\text{Rh}_4(\text{CO})_1$	$C_s$	1CO- $C_s$	0.0834	-553.8046	-553.8059	-553.8166	<b>-553.8186</b>	<i>i</i>	-113.7	-114.0
$\text{Rh}_4(\text{CO})_2$	$C_s$	2CO- $C_s$	0.1667	-667.2131	-667.2270	<b>-667.2331</b>	-667.2304	-667.1791	-111.4	-109.0
$\text{Rh}_4(\text{CO})_2$	$C_1$	2CO- $C_1$	0.1667	-667.2317	-667.2372	<b>-667.2395</b>	-667.2305	-667.1854	-119.9	-121.5
$\text{Rh}_4(\text{CO})_3$	$C_s$	3CO- $C_s$	0.2500	-780.6159	<b>-780.6403</b>	-780.6366	-780.6208		-104.3	-104.0
$\text{Rh}_4(\text{CO})_3$	$C_1$	3CO- $C_1$	0.2500	-780.6576	<b>-780.6604</b>	-780.6561	-780.6395		-121.9	-124.0
$\text{Rh}_4(\text{CO})_4$	$C_2$	4CO- $C_2$	0.3334	<b>-894.0912</b>	-894.0725	-894.0552	-894.0405	<i>e</i>	-129.4	-129.0
$\text{Rh}_4(\text{CO})_5$	$C_1$	5CO- $C_1$	0.4167	<b>-1007.5056</b>	-1007.4970				-125.3	-122.2
$\text{Rh}_4(\text{CO})_6$	$C_2$	6CO- $C_2$	0.5000	<b>-1120.8984</b>	-1120.8807	<i>h</i>			-113.1	-112.7
$\text{Rh}_4(\text{CO})_8$	$S_4$	8CO- $S_4$	0.6667	<b>-1347.7059</b>	<i>f</i>	<i>f</i>			-105.1	-104.5
$\text{Rh}_4(\text{CO})_9$	$C_{3v}$	9CO- $C_{3v}$	0.7500	<b>-1461.0878</b>	<i>g</i>	<i>g</i>			-96.0	-96.3
$\text{Rh}_4(\text{CO})_{12}$	$T_d$	12CO- $T_d$	1.0000	<b>-1801.2230</b>	<i>d</i>	<i>d</i>			-75.6	-80.0
$\text{Rh}_4$	$C_s$	$\text{Rh}_4$ - $C_s$	n/a	-440.3871	-440.3845	-440.3868	<b>-440.4024</b>	<i>i</i>	n/a	n/a
CO	$D_{\infty h}$	CO-	n/a	<b>-113.3729</b>					n/a	n/a

<sup>a</sup>The rightmost columns present the average free energy of CO adsorption as derived from DFT and the model given in eq 5. The lowest energy states are shown in bold. <sup>b</sup>The 3D structures of the lowest energy complexes are given in Figure 2. <sup>c</sup>The surface coverage ( $\theta = 1$ ) has been defined on the basis of eq 2. <sup>d</sup>Relaxed to  $\text{Rh}_4(\mu\text{-CO})_3(\text{CO})_9$ . <sup>e</sup>Relaxed to  $\text{Rh}_4(\mu\text{-CO})(\text{CO})_3$ . <sup>f</sup>Relaxed to  $\text{Rh}_4(\mu\text{-CO})_4(\text{CO})_4$ . <sup>g</sup>Relaxed to  $\text{Rh}_4(\mu\text{-CO})_4(\text{CO})_5$ . <sup>h</sup>Relaxed to  $\text{Rh}_4(\mu\text{-CO})_2(\text{CO})_4$ . <sup>i</sup>Minimum could not be located.

following stoichiometries (label):  $\text{Rh}_4\text{CO}$  (1CO- $C_s$ ),  $\text{Rh}_4(\text{CO})_2$  (2CO- $C_1$ ),  $\text{Rh}_4(\text{CO})_2$  (2CO- $C_s$ ),  $\text{Rh}_4(\text{CO})_3$  (3CO- $C_1$ ),  $\text{Rh}_4(\text{CO})_3$  (3CO- $C_s$ ),  $\text{Rh}_4(\text{CO})_4$  (4CO- $C_2$ ),  $\text{Rh}_4(\text{CO})_5$  (5CO- $C_1$ ),  $\text{Rh}_4(\text{CO})_6$  (6CO- $C_2$ ),  $\text{Rh}_4(\text{CO})_8$  (8CO- $S_4$ ),  $\text{Rh}_4(\text{CO})_9$  (9CO- $C_{3v}$ ) and  $\text{Rh}_4(\text{CO})_{12}$  (12CO- $T_d$ ) (Figure 2). The  $\text{Rh}_4(3,1)$  nanocluster had a perfect  $T_d$  geometry, and CO was attached to it at nearly  $90^\circ$  with respect to the cluster facet surface. Previously, we have shown that such a nanocluster with various adsorbed CO species is adequate for the spectral assignment of the vibrational bands observed in diffuse reflectance infrared Fourier-transform (DRIFTS) spectra of  $\text{Rh}/\text{Al}_2\text{O}_3$ <sup>31</sup> exposed to a feedstream of CO. The structures were located through multiple optimization runs, making use of successive lower point group symmetries and spin multiplicities (SM) of 1, 3, 5, 7, and 9. For instance, the fully saturated complex (12CO- $T_d$ ), was first optimized using the highest possible point group symmetry ( $T_d$ ), resulting in three weak imaginary frequencies (55.5i, 34.7i, 10.3i). These, after optimization at the lower symmetry point group ( $C_s$ ) resulted in a local minimum. A similar weak distortion was observed for 4CO- $C_2$  and 9CO- $C_{3v}$  with a doubly degenerate imaginary frequency of 39.6i and 27.5i, respectively, where the point group symmetry had to be reduced to the  $C_s$  point group, to locate a local minimum.

The optimized geometries for the models with the lowest energy and their corresponding total free energies as a function of SM are presented in Figure 2 and Table 1, respectively. Certain structural perturbations have been observed by monitoring the adsorption-induced bond length alterations to the cluster and the M-CO bond. In 1CO- $C_s$  we observed a dramatic 13.2% adsorption induced bond elongation for the Rh-Rh bond with the largest projection on the Rh-CO bond, whereas, for Rh-Rh bonds with smaller projections on the Rh-CO bond, a bond elongation of only 0.6% was observed, in both cases, compared to the average Rh-Rh bond length of the bare  $\text{Rh}_4(3,1)$  cluster (2.578 Å). This indicates that the adsorption of CO on metal clusters significantly weakens the metal-metal bonds, in agreement with previous studies that

presented CO adsorption-induced decomposition of the metal cluster at various temperatures, including room temperature.<sup>65</sup> Comparison of the structures of 1CO- $C_s$ , 2CO- $C_s$ , and 3CO- $C_s$  yielded the following structural perturbations upon successive CO adsorption: (i) the carbon-oxygen (C-O) bond length, 1.150, 1.147, and 1.144 Å, respectively, decreases and (ii) the Rh-Rh bond length that has the smallest projection on the C-O axis, 2.919, 2.702, and 2.588 Å, respectively, decreases, both of which are in agreement with a decrease of the adsorption energy of CO. The increase of the Rh-Rh bond length upon adsorption is supportive of the view that there is electron transfer through the  $\pi$ -back-donation mechanism from occupied orbitals that bind the two metals to empty orbitals at the carbon-end of CO, which according to the MO diagram in Figure 1, could be either the  $6\sigma^*$  or the doubly degenerate  $2\pi^*$  MOs. However, because the  $6\sigma^*$  is essentially shielded by the electron density of the occupied  $5\sigma$  state, only the  $2\pi^*$  states are essentially expected to accept electron density through the  $\pi$ -back-donation mechanism. Based on these structural observations, it is suggestive that the  $\pi$ -back-donation bond formation is sensitive not only to the effective electron transfer of electron density of the chemical bonds that are connected to the metal atom where CO is bound but also to the relative orientation of the chemical bonds with respect to the direction in which the charge transfer occurs. We will further support this view through electron density difference plots and electrostatic potential plots in subsequent sections that reveal that spatial redistribution of the electron density as a result of the electron transfer  $\pi$ -back-donation mechanism is evident in the examined cases.

**Coverage-Dependent Adsorption Energy.** The coverage-dependent adsorption energy of CO on  $\text{Rh}_4(3,1)$  was calculated using high-symmetry clusters of the form  $\text{Rh}_4(\text{CO})_n$ , where  $n = 1-9$  and 12, shown in Figure 2. The corresponding Gibbs free energy change per CO ( $\Delta G_{\text{CO}}^\circ$ ) for the adsorption of carbon monoxide on  $\text{Rh}_4(3,1)$  as a function of  $\theta_{\text{CO}}$  are also tabulated in Table 1 and plotted in Figure 3.

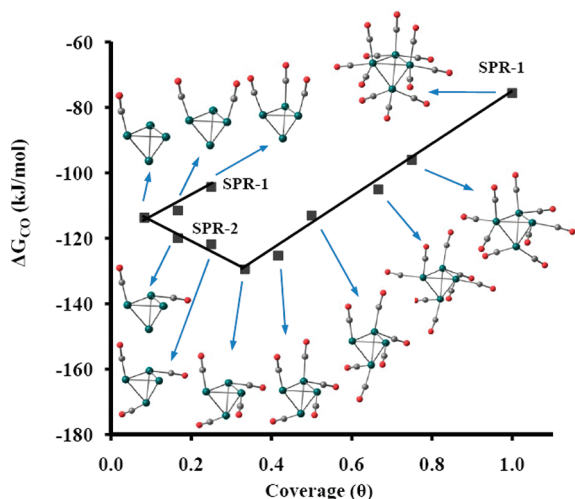


**Figure 3.** Gibbs free energy change ( $\Delta G_{\text{CO}}^{\circ}$ ) per CO for the adsorption of carbon monoxide on  $\text{Rh}_4(3,1)$  as a function of  $\theta_{\text{CO}}$ , calculated using eqs 1 and 2, respectively. The data points of this plot are given in Table 1.

Our results indicated that an increase of the surface coverage quenches the magnetic moment of the cluster. This can be seen by observing the spin multiplicity of the lowest energy cluster/adsorbate model, which at low coverages (0.0834) is  $\text{SM} = 7$ , identical to that for the bare cluster, whereas at coverages higher than 1/3 the magnetic properties are completely quenched to a closed shell spin configuration ( $\text{SM} = 1$ ). This is in agreement with molecular beam deflection experiments on nickel clusters, which upon CO adsorption exhibit a decrease in their magnetic moments of 6 bohr magnetons.<sup>66</sup>

Another important observation that emerged from this data set is the dramatic range (54 kJ/mol) that the adsorption free energy per CO molecule can have, if for example, one compares the values for  $4\text{CO-C}_2$  (−129 kJ/mol) to that of  $12\text{CO-T}_d$  (−76 kJ/mol). By comparison of these adsorption energies, it becomes evident that the free energy of adsorption of CO at high  $\theta_{\text{CO}}$  ( $12\text{CO-T}_d$ ) can be 40% weaker than the adsorption energy at lower  $\theta_{\text{CO}}$  ( $4\text{CO-C}_2$ ). It is generally accepted that the adsorption energy on small clusters is usually higher at low coverages; however, little is known about the underlying reason that causes this dramatic coverage-dependent adsorption energy enhancement. From the results in Figure 3 we observe that if CO is added to the cluster in a systematic fashion, then certain structure–property relationships (SPR) start to appear. We further analyzed these SPR to understand the origin of the strong variations seen in the average adsorption free energy of CO to the rhodium cluster and the nonintuitive inverse coverage-dependent trends observed comparing SPR-1 and SPR-2. Our subsequent analysis is intended to explain these variations through a simplistic semiquantitative model.

SPR-1 (for convenience we use the same label for both lines regardless if the slope is not exactly the same) shows that there is a near linear increase of the adsorption energy (becoming less exothermic) as a function of  $\theta_{\text{CO}}$ . This trend is in accordance with the trend observed on extended surfaces, usually attributed to repulsive dipole–dipole interactions between CO molecules that weaken the M–CO bond.<sup>67</sup> An intriguing result is the exact opposite trend observed in SPR-2. There, we observe an increase of the adsorption energy as a function of  $\theta_{\text{CO}}$ . In SPR-2 we have a complete absence of CO repulsions as COs are not

adsorbed in parallel configuration or on the same metal atom (i.e., dicarbonyls, tricarbonyls); therefore, an additional effect changes the adsorption energy which can only be explained by the introduction of an additional attractive interaction labeled as the adsorbate–metal–metal–adsorbate bond (A-M-M-A).

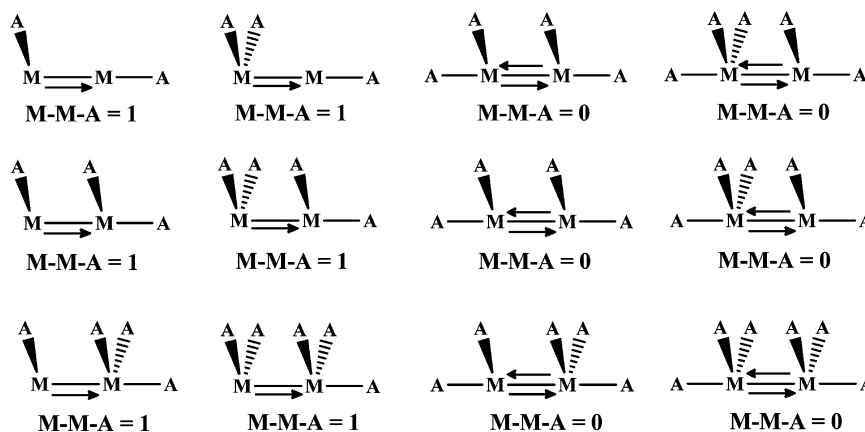
In our simplistic model we assume that during the adsorption of CO on the small cluster there are four interactions that affect the average free energy of CO adsorption ( $\Delta G_{\text{CO}}^{\circ}$ ): (i) adsorbate–metal interaction ( $E_{\text{A-M}}$ ), which is the attractive energy due to the metal–carbonyl bond formation, (ii) adsorbate–adsorbate interaction ( $E_{\text{A-A}}$ ), which is the repulsive energy between COs placed in parallel configuration on adjacent metals, (iii) adsorbate–metal–adsorbate interaction ( $E_{\text{A-M-A}}$ ), which is the repulsive interaction between COs adsorbed to the same metal center (i.e., dicarbonyl and tricarbonyl species), and (iv) adsorbate–metal–metal–adsorbate ( $E_{\text{A-M-M-A}}$ ) interaction, in which one CO bond is collinear with the metal–metal bond and the second CO is residing on an adjacent metal atom at a  $\approx 90^\circ$  angle. The adsorption of the second CO is stronger as a result of the metal–metal bond polarization in the direction of the M–CO bond (we provide detailed evidence of this interaction in the subsequent sections). Using these four parameters, we fit the following equation to our calculated data through root-mean-square-difference (rmsd) minimization.

$$\Delta G_{\text{CO}}^{\circ} = -a \cdot E_{\text{A-M}} + b \cdot E_{\text{A-A}} + c \cdot E_{\text{A-M-A}} - d \cdot E_{\text{A-M-M-A}} \quad (5)$$

where  $a$ ,  $b$ ,  $c$ , and  $d$  are the numbers of A-M, A-A, A-M-A, and A-M-M-A moieties, respectively (given as Supporting Information in S-Table 2).

The model values reproduce relatively well the calculated DFT values (see last two columns in Table 1), as indicated by the small rmsd = 1.45. It is noted that without consideration of the A-M-M-A interactions, this agreement is much weaker (rmsd = 5.91). We have applied this model to other  $\text{Rh}_4(3,1)(\text{CO})_n$  models, where  $n = 5-7$  but with configurations different from the ones presented, and it reproduces the average adsorption energies to within less than 1–10%. Therefore, we support the view that within the model systems examined here, it is necessary to include this additional attractive stabilization that is generated by the polarization of the metal–metal bonds (A-M-M-A parameter) of the cluster to reach better agreement with the DFT results. We show that the additional stabilization of the cluster CO model occurs when the configuration of COs is such that metal–metal bond polarization can occur, favoring the  $\pi$ -back-donation mechanism and facilitating stronger adsorption of the neighboring adsorbate. In this CO configuration, the CO on one metal atom is collinear with a metal–metal bond and a second CO is adsorbed vertical to the metal–metal bond, at the second metal atom (see in Figure 2,  $2\text{CO-C}_1$ ). When two such configurations are present on the same metal bond, they cancel out, as the polarization of the first is counter-polarized by the second running in the opposite direction. When one configuration is present, the polarization of the metal–metal bond decreases the Pauli repulsion for the second adsorbate and maximizes the overlap between filled states of the metal and the empty  $2\pi^*$  states of CO, forming a relatively stronger M–CO bond. Furthermore, it is possible that the polarization generates a partial negative charge on metal 1, which then enhances the strength of the metal–CO bond that is collinear with the metal–metal bond. Both these effects can be rationalized by careful consideration of bond

Scheme 1. Schematic Representation of the Various Rhodium–CO Configurations That Yield the Metal–Metal Bond Polarization That Enhances the Average CO Adsorption Energy on the Cluster



length alternations upon adsorption and by observation of the electron density difference plots, shown in Figure 6. The numbering for the A-M-M-A moieties on the models examined is described in Scheme 1.

From the semiquantitative model that we derived we found that the most important attractive interaction is the formation of the metal–carbonyl bond, which had a fitted value of A-M = 114 kJ/mol per CO. The cluster is further stabilized by the A-M-M-A interactions that were found to be 1 order of magnitude lower (A-M-M-A = 15 kJ/mol) than the A-M interactions. These attractive interactions are reduced by other coverage-dependent repulsions between adsorbed COs. In particular, the repulsive energy between COs in dicarbonyl and tricarbonyl species was found to be A-M-A = 24 kJ/mol, whereas the repulsive energy between parallel adsorbed COs on adjacent metals was found to be A-A = 10 kJ/mol. These values clearly show that the repulsive interactions between CO moieties on the cluster are 5–10 times smaller than the attractive interactions due to the formation of the metal–carbonyl bond.

It is interesting to notice that these results support the picture that repulsive energy between COs is further enhanced during the adsorption induced dipole that is formed upon CO adsorption. This can be clearly seen in the electrostatic potential maps obtained in Figure 6 but is also evident from energetic arguments, outlined in the following paragraph. To get an accurate estimate of the repulsive CO interactions prior adsorption, we performed high-level coupled cluster calculations, shown in Figure 4.

This figure shows that at distances larger than 3.5 Å there is an absence of repulsive interactions. For extended surfaces, if one assumes only atop or hollow adsorption on the Rh(111) surface, at  $\theta_{\text{CO}} = 1$ , the nearest-neighbor distance is 2.689 Å, based on the cubic close-packed (ccp) crystal structure of rhodium,<sup>68</sup> which corresponds to a repulsive energy of 25 kJ/mol. However, due to the spherical geometry of the CO adsorption shell examined here, the nearest-neighbor distance between CO molecules ranges between 3.2 and 3.6 Å, which corresponds to a repulsive energy of less than 2 kJ/mol, significantly lower than the one we find in our model. This suggests that the repulsive energy between COs is further enhanced upon adsorption, due to adsorption-induced dipole–dipole electrostatics or the presence of a metal surface, which promotes electron-delocalization<sup>25</sup> of the diffuse metal electron density, offered to CO, through the  $\pi$ -back-donation

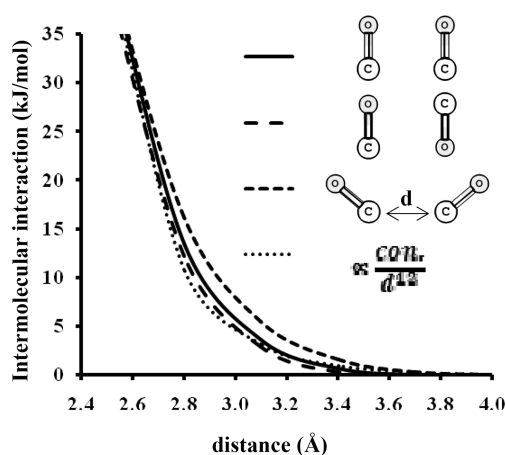


Figure 4. Intermolecular interaction between relaxed carbon monoxide dimer in parallel, antiparallel, and bent configurations obtained using CCSD(T)/aug-cc-pVTZ. A repulsive VdW commonly used in Lennard-Jones (12-6) potential is shown for comparison. The intermolecular interaction was calculated using  $E_{\text{int}}(r) = E_{\text{CO-CO}} - 2E_{\text{CO}}$ .

mechanism. Electrostatic potential maps in the last section of this paper provide further evidence of the adsorption-induced dipole formed during adsorption.

**Infrared Absorption Spectra Simulations.** Even though the evolution of infrared (IR) absorption or transmittance peaks as a function of  $\theta_{\text{CO}}$  is an extensively studied topic on surfaces, very little is known about the coverage-dependent evolution of IR bands on nanoclusters. Therefore, in this section we explore the evolution of the IR absorption bands of the rhodium carbonyl cluster, as a function of  $\theta_{\text{CO}}$ . The IR intensity of each vibrational mode  $i$  was taken to be proportional to the square of the derivative of the molecular dipole field with respect to the vibrational coordinate ( $q_i$ ) given by

$$I_{0 \rightarrow 1} = \left[ \int \psi_{\nu=0} \frac{\partial \mu}{\partial q_i} \psi_{\nu=1} dq_i \right]^2 \quad (6)$$

where the harmonic oscillator wave functions are used for  $\psi_{\nu=0}$  and  $\psi_{\nu=1}$ . The dipole derivatives were calculated analytically, together with the force constants from the DFT wave functions.<sup>69</sup> In Figure 5, the simulated infrared absorbance

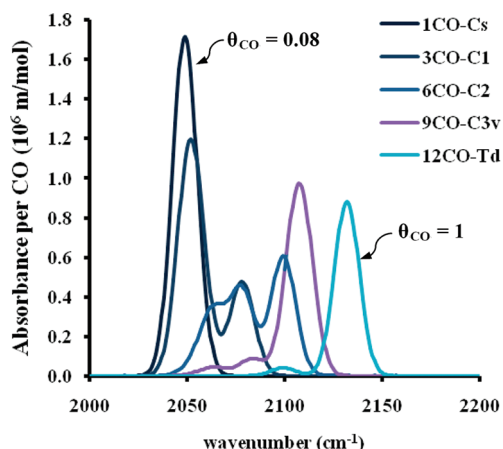


**Figure 5.** Simulated infrared absorbance spectra (normalized per CO) for various rhodium carbonyl clusters, showing symmetric and antisymmetric carbon–oxygen (C–O) stretching vibrations, as a function of  $\theta_{\text{CO}}$ .

spectra of the various rhodium–carbonyl clusters examined, are presented. The infrared spectra clearly show the existence of a strong absorption band located at  $2075 \pm 80 \text{ cm}^{-1}$ , which corresponds to various antisymmetric and symmetric vibrational stretching modes of the C–O bond. The relative location of this band on the frequency scale appears to be very sensitive to  $\theta_{\text{CO}}$ . In particular, at  $\theta_{\text{CO}} \approx 0.08$  this band is located at  $2047 \text{ cm}^{-1}$ , whereas at  $\theta_{\text{CO}} = 1$ , the same band is blue-shifted by  $80 \text{ cm}^{-1}$ . This frequency blue shift upon CO adsorption has been

previously attributed to repulsive dipole–dipole interactions between adjacent CO groups on extended surfaces that cause coupling of vibrational groups, splitting the band that corresponds to linear-CO, into a doublet.<sup>70,71</sup> On a nanocluster we observe that the vibrational band for 1-CO may split into as many as three bands (i.e., A and 2B for 6CO-C<sub>2</sub>), which corresponds to the coupling of 1-CO in parallel configuration<sup>31</sup> and the coupling of dicarbonyl species.<sup>2</sup> This shift in the frequencies corresponds also to drastic changes in the adsorption free energy as we have presented in the previous section of this paper. This suggests that increase of  $\theta_{\text{CO}}$  causes strengthening of the C–O bond, which is usually attributed to the weakening of the M–CO bond.<sup>31</sup> The ratio of  $\Delta G_{\text{CO}}^{\circ}/\Delta\nu$  ( $0.5 \text{ kJ}\cdot\text{cm}/\text{mol}$ ) yields a rough estimate of the adsorption energy change via monitoring the frequency shift in IR spectra of rhodium nanoclusters. The relative magnitude of this value clearly demonstrates the sensitivity of infrared spectroscopic techniques in their use of obtaining energetic information of CO on metal nanoclusters. A similar blue shift of  $80\text{--}100 \text{ cm}^{-1}$  is also observed for the metal–carbonyl stretching and bending modes (not shown), which appear in a band between  $380\text{--}520 \text{ cm}^{-1}$  and are 10-fold weaker in intensity than the corresponding C–O stretching bands. Finally, we observed a decrease of the integrated area of the absorbance bands normalized per CO, as a function of  $\theta_{\text{CO}}$ . A similar decrease of the IR absorption intensity has been observed in a previous study, where through variation of the degree of  $\pi$ -backdonation, by changing the metal atom of the adsorption site, a gradual decrease of the IR absorption intensity has been observed.<sup>11</sup> We note that the coverage-dependent blue shift of

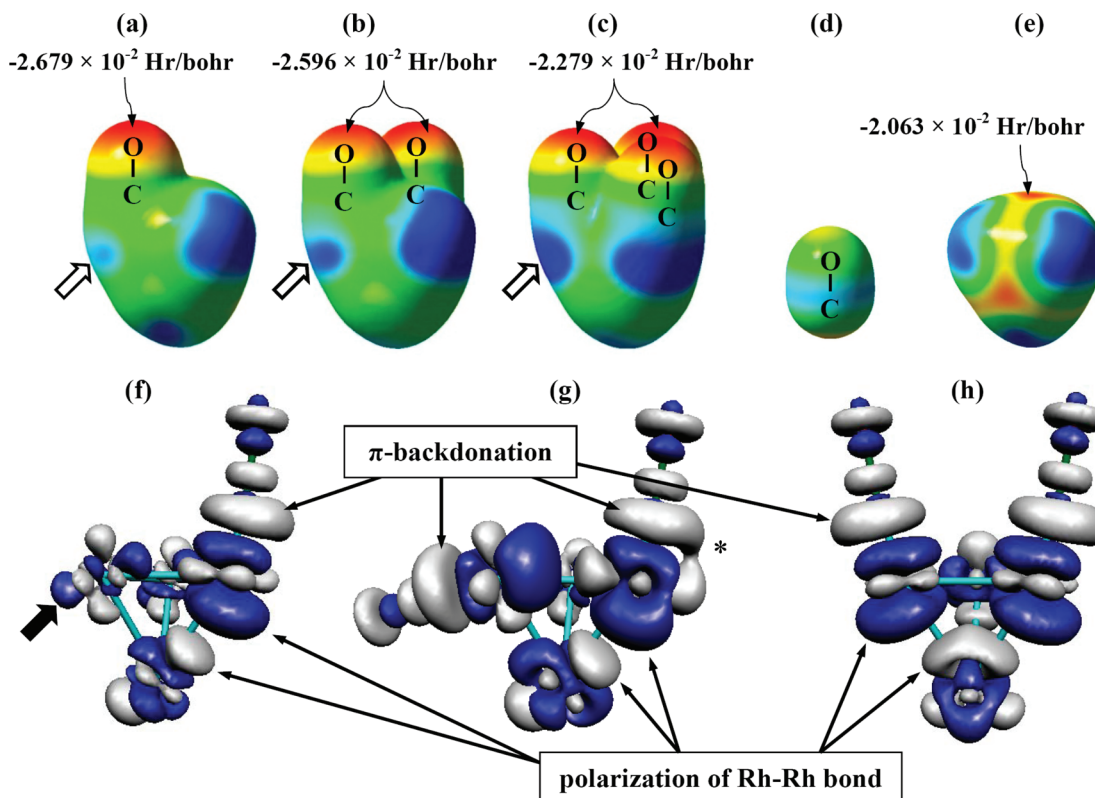


**Figure 6.** Molecular electrostatic potential of (a) 1CO-C<sub>s</sub>, (b) 2CO-C<sub>s</sub>, (c) 3CO-C<sub>s</sub>, (d) CO, and (e) Rh<sub>4</sub>(3,1) and electron density difference plots of (f) 1CO-C<sub>s</sub>, (g) 2CO-C<sub>1</sub>, and (h) 2CO-C<sub>s</sub>, generated on a 0.0004 and 0.005 e/au<sup>3</sup> isodensity surface, respectively. Dark regions in (a)–(e) correspond to a positive electrostatic potential and in (f)–(h) to a decrease of electron density, respectively. Isosurfaces were obtained on a 0.1 Å grid.

the vibrations band of CO maybe an interesting property in the utilization of metal nanoclusters as trace-gas sensors.

**Electron Density Difference and Electrostatic Potential Plots.** In this section we provide further evidence concerning the A-M-M-A bond, to rationalize the two very different trends (SPR-1, SPR-2) observed concerning the adsorption energy of CO as a function of  $\theta_{\text{CO}}$ . For this, we perform an in-depth investigation of the molecular electrostatic potential (ESP), before and after adsorption, and generate electron density difference plots ( $\rho_{\text{diff}}$ ) to show the adsorption induced electron density perturbations, in both the metal cluster and the adsorbate. The molecular electrostatic potentials were obtained by the evaluation of the potential of a positive point charge on a 0.0004 e/au<sup>3</sup> isodensity surface whereas, the electron density difference plots were calculated using the following equation,

$$\rho_{\text{diff}} = \int \Psi_{\text{Rh}_4(\text{CO})_n}^2 d\tau - \int \Psi_{\text{Rh}_4}^2 d\tau - \int \Psi_{(\text{CO})_n}^2 d\tau \quad (7)$$

where the first term corresponds to the electron density of the metal–carbonyl complex, the second term to the electron density of the metal particle in the presence of the adsorbate ghost atoms, and the last term to the CO adsorption shell with the metal particle replaced by ghost atoms. These isodensity values were critical to reveal the adsorption-induced electron transfer processes (i.e.,  $\pi$ -back-donation, metal–metal polarization), which are more apparent in the diffuse electron density region of the models examined. A very interesting aspect of the ESP plots presented is that prior to adsorption (Figure 6d), only a very weak negative electrostatic potential at the carbon end is observed, indicative of little polarization, and in agreement with the small dipole moment (0.112 D,  $3.74 \times 10^{-31}$  C·m)<sup>72</sup> of gas phase CO. The rhodium nanocluster, on the other hand, appears to have a positive electrostatic potential at each rhodium atom whereas hollow and bridge sites possess a negative electrostatic potential. The situation changes drastically when adsorption of CO occurs, as CO (Figure 6a–c) and especially oxygen, develop a prominent negative electrostatic potential, indicative of substantial charge transfer from the metal cluster to the adsorbate and the formation of an adsorption-induced dipole,  $\text{C}^{\delta+}-\text{O}^{\delta-}$ . At the same time, there is an increase of the positive electrostatic potential at the Rh atom (see arrow in Figure 6a–c), which indicates the development of a positive charge at the metal, as a result of the charge transfer to the adsorbates. The negative electrostatic potential at the CO moieties decreases as a function of CO surface coverage (Figure 6a–c), indicating that the mechanism of charge transfer becomes less efficient as the number of adsorbates increases, due to repulsive A-A interactions. The exact mechanism of the charge transfer can be visualized in the electron density difference plots presented in Figure 6f–g. It is evident that for the examples presented, the metal–carbonyl bond for atop adsorbed CO occurs by the simultaneous electron donation of the  $\pi$  bond electron density, belonging to the metal–metal  $\pi$ -bond, into the empty  $2\pi^*$  MO of CO. This causes partial disruption of the metal–metal  $\pi$  bonds that have their axis of symmetry almost colinear with the M–CO bond. This observation is in fact reasonable in the light that  $\pi$  states are generally more polarizable along chemical bonds, as we have recently shown to be the underlying reason for the nonlinear static longitudinal polarizability of polyynes<sup>73,74</sup> and polyacenes.<sup>75</sup> In contrast, the chemical metal–metal bonds that are

almost perpendicular to the metal–CO bond undergo less electron transfer to the  $2\pi^*$  MO of CO. We, therefore, found that the electron transfer direction of metal d-electron density into the  $2\pi^*$  MO of CO is closely correlated to the direction in which the metal–metal bonds of the cluster can more effectively polarize. The polarization of the metal–metal bonds can be clearly seen in the  $\rho_{\text{diff}}$  plots presented in Figure 6f,g,h. We note that the polarizability of  $\pi$ -bonds in metal clusters appears to be a critical parameter that determines the strength of the A-M interactions.

In particular, in Figure 6f the adsorption of the first CO facilitates larger polarization of the Rh–Rh bond with a larger projection on the M–CO bond. Therefore, adsorption of subsequent CO molecules is favored at a position (shown by filled arrow, Figure 6f) where the polarization caused by the second adsorbate will stabilize the polarization caused by the first. Therefore, the adsorption of CO as shown for SPR-2 will result in higher adsorption energies. The adsorption of the second adsorbate in Figure 6g, also increases the amount of  $\pi$ -back-donation, indicated by the bulkier negative electron density region on the carbon atom (see asterisk in Figure 6g). By monitoring the relative volume of the  $\pi$ -back-donation isosurface, we observe that there is a gradual decrease of this isodensity volume, in agreement with the trend observed in SPR-1 and indicative of a less efficient charge transfer through the  $\pi$ -back-donation mechanism, as a function of  $\theta_{\text{CO}}$ .

## CONCLUSIONS

A systematic computational study of carbon monoxide adsorption on a tetrahedral rhodium cluster,  $\text{Rh}_4(3,1)$ , is presented in this work. Two coverage-dependent structure–property relationships concerning the adsorption energy of CO of opposing trend, were found. The first, in agreement with the coverage-dependent adsorption characteristics of CO on extended metal surfaces, resulted in lowering of the adsorption energy as a function of coverage. The second, only present at low coverages ( $\theta < 0.3$ ), was found to have the exact opposite trend. The coverage-dependent adsorption energy trends are rationalized through the derivation of a *semiquantitative model* and further supported through molecular orbital energy diagrams, electron density difference plots, molecular electrostatic potential plots and simulated infrared spectra that show that attractive *adsorbate–metal–metal–adsorbate interactions* are considerably strong (25 kJ/mol per CO) at low coverages on metal nanoclusters.

Certain additional useful observations and conclusions are derived, which are listed below: (i) the  $\pi$ -back-donation bond formation is sensitive not only to the effective electron transfer of electron density of the chemical bonds that are connected to the metal atom where CO is bound but also to the relative orientation of the chemical bonds with respect to the direction in which the charge transfer occurs, (ii) the ratio of the adsorption energy per CO divided by the infrared shift was found to be 0.45 kJcm/mol, useful for the assessment of adsorption energy changes of CO from  $\text{Rh}_4(3,1)$  using infrared band shifts, (iii) the coverage-dependent blue shift of the vibrations band of CO may be an interesting property in the utilization of metal nanoclusters as trace-gas sensors, (iv) adsorbate–adsorbate interactions during the adsorption of CO to  $\text{Rh}_4(3,1)$  are 5–10 times weaker than the metal–carbonyl bond strength, the latter dominating the adsorption energetics, and (v) electrostatic potential plots clearly show that there is an adsorption induced dipole generated due to effective charge

transfer from the metal  $\pi$ -bonding system to the  $2\pi^*$  MO of CO.

## ■ ASSOCIATED CONTENT

### ■ Supporting Information

Cartesian coordinates of all optimized geometries and the number of A-M, A-A, A-M-A, and A-M-M-A moieties for each model, respectively are given in S-Table 1 and S-Table 2, respectively. This material is available free of charge via the Internet at <http://pubs.acs.org>.

## ■ AUTHOR INFORMATION

### Corresponding Author

\*E-mail: [zeinalip@insilicotech.com](mailto:zeinalip@insilicotech.com).

### Notes

The authors declare no competing financial interest.

## ■ ACKNOWLEDGMENTS

The authors acknowledge Dr. Eriketi Z. Loizidou proofreading this paper and Prof. Andrew L. Cooksy for useful discussions.

## ■ REFERENCES

- (1) Yates, J. T. Jr.; Gelin, P.; Beebe, T. P., Jr. *IR Spectroscopic Characterization of Adsorbed Species and Processes on Surfaces*; Division of Colloid and Surface Chemistry: American Chemical Society: Philadelphia, PA, 1984; Vol. August.
- (2) Yates, J. T., Jr.; Duncan, T. M.; Worley, S. D.; Vaughan, R. W. *J. Chem. Phys.* **1979**, *70*, 1219–1224.
- (3) Blyholder, G. *J. Phys. Chem. B* **1964**, *68*, 2772–2777.
- (4) Bagus, P. S.; Nelin, C. J.; Bauschlicher, C. W. *Phys. Rev. B* **1983**, *28*, 5423–5438.
- (5) Bagus, P. S.; Hermann, K. *Phys. Rev. B* **1986**, *33*, 2987.
- (6) Sung, S. S.; Hoffmann, R. *J. Am. Chem. Soc.* **1985**, *107*, 578–584.
- (7) Föhlisch, A.; Nyberg, M.; Bennich, P.; Triguero, L.; Hasselström, J.; Karis, O.; Pettersson, L. G. M.; Nilsson, A. *J. Chem. Phys.* **2000**, *112*, 1946.
- (8) Föhlisch, A.; Nyberg, M.; Hasselström, J.; Karis, O.; Pettersson, L. G. M.; Nilsson, A. *Phys. Rev. Lett.* **2000**, *85*, 3309.
- (9) Nilsson, A.; Pettersson, L. G. M. *Surf. Sci. Rep.* **2004**, *55*, 49–167.
- (10) Hammer, B.; Morikawa, Y.; Norskov, J. K. *Phys. Rev. Lett.* **1996**, *76*, 2141–2144.
- (11) Zeinalipour-Yazdi, C. D.; Cooksy, A. L.; Efstathiou, A. M. *Surf. Sci.* **2008**, *602*, 1858–1862.
- (12) Waszczuk, P.; Wieckowski, A.; Zelenay, P.; Gottesfeld, S.; Coutanceau, C.; Léger, J. M.; Lamy, C. *J. Electroanal. Chem.* **2001**, *511*, 55–64.
- (13) Kang, K.-S.; Lee, S. P. *J. Mater. Sci.* **2003**, *38*, 4319–4323.
- (14) Xie, X. W.; Li, Y.; Liu, Z. Q.; Haruta, M.; Shen, W. *Nature* **2009**, *458*, 746.
- (15) Fu, Q.; Weber, A.; Flytzani-Stephanopoulos, M. *Catal. Lett.* **2001**, *77*, 87–95.
- (16) Zeinalipour-Yazdi, C. D.; Efstathiou, A. M. *J. Phys. Chem. C* **2008**, *112*, 19030–19039.
- (17) Fischer, F.; Tropsch, H. *Ber. Dtsch. Chem. Ges.* **1926**, *59*, 830.
- (18) Tao, F.; Dag, S.; Wang, L.-W.; Liu, Z.; Butcher, D. R.; Bluhm, H.; Salmeron, M.; Somorjai, G. A. *Science* **2010**, *327*, 850–853.
- (19) Fu, Q.; Saltsburg, H.; Flytzani-Stephanopoulos, M. *Science* **2003**, *301*, 935–938.
- (20) Rae, S.; Khan, I. *Analyst* **2010**, *135*, 1365–1369.
- (21) Little, L. H. *Infrared spectra of adsorbed species*; Academic: London, 1966.
- (22) Hair, M. L. *Infrared spectroscopy in surface chemistry*; Marcel Dekker: New York, 1967.
- (23) Gajdos, M.; Eichler, A.; Hafner, J.; Meyer, G.; Rieder, K. H. *Phys. Rev. B* **2005**, *71*, 7.
- (24) German, E. D.; Sheintuch, M. *J. Phys. Chem. C* **2008**, *112*, 14377–14384.
- (25) Mason, S. E.; Grinberg, I.; Rappe, A. M. *J. Phys. Chem. B* **2006**, *110*, 3816–3822.
- (26) Mason, S. E.; Grinberg, I.; Rappe, A. M. *Phys. Rev. B* **2004**, *69*.
- (27) Hussain, A.; Ferre, D. C.; Gracia, J.; Nieuwenhuys, B. E.; Niemantsverdriet, J. W. *Surf. Sci.* **2009**, *603*, 2734–2741.
- (28) Mehmood, F.; Kara, A.; Rahman, T. S.; Henry, C. R. *Phys. Rev. B* **2009**, *79*, 6.
- (29) Mehmood, F.; Kara, A.; Rahman, T. S.; Bohnen, K. P. *Phys. Rev. B* **2006**, *74*, 9.
- (30) Mojet, B. L.; Miller, J. T.; Koningsberger, D. C. *J. Phys. Chem. B* **1999**, *103*, 2724–2734.
- (31) Zeinalipour-Yazdi, C. D.; Cooksy, A. L.; Efstathiou, A. M. *J. Phys. Chem. C* **2007**, *11*, 13872–13878.
- (32) Zhou, J.; Li, Z. H.; Wang, W. N.; Fan, K. N. *J. Phys. Chem. A* **2006**, *110*, 7167–7172.
- (33) Poater, A.; Duran, M.; Jaque, P.; Toro-Labbe, A.; Sola, M. *J. Phys. Chem. B* **2006**, *110*, 6526–6536.
- (34) Mineva, T.; Russo, N.; Freund, H. J. *J. Phys. Chem. A* **2001**, *105*, 10723–10730.
- (35) Pacchioni, G.; Bagus, P. S. *J. Chem. Phys.* **1990**, *93*, 1209–1214.
- (36) German, E. D.; Sheintuch, M.; Kuznetsov, A. M. *J. Phys. Chem. C* **2008**, *112*, 15510–15516.
- (37) Scheijen, F. J. E.; Ferre, D. C.; Niemantsverdriet, J. W. *J. Phys. Chem. C* **2009**, *113*, 11041–11049.
- (38) Sorescu, D. C. *J. Phys. Chem. C* **2008**, *112*, 10472–10489.
- (39) Lo, J. M. H.; Ziegler, T. *J. Phys. Chem. C* **2008**, *112*, 9114–9114.
- (40) Lo, J. M. H.; Ziegler, T. *J. Phys. Chem. C* **2008**, *112*, 3692–3700.
- (41) Liu, Z. P.; Hu, P. *J. Chem. Phys.* **2001**, *114*, 8244–8247.
- (42) Demirci, E.; Carbogno, C.; Gross, A.; Winkler, A. *Phys. Rev. B* **2009**, *80*, 13.
- (43) Sumer, A.; Aksoylu, A. E. *J. Phys. Chem. C* **2009**, *113*, 14329–14334.
- (44) Termentzidis, K.; Hafner, J. *J. Phys.-Condens. Matter* **2007**, *19*, 7.
- (45) Sakong, S.; Mosch, C.; Gross, A. *Phys. Chem. Chem. Phys.* **2007**, *9*, 2216–2225.
- (46) Orita, H.; Inada, Y. *J. Phys. Chem. B* **2005**, *109*, 22469–22475.
- (47) Bromfield, T. C.; Ferre, D. C.; Niemantsverdriet, J. W. *Chem. Phys. Chem.* **2005**, *6*, 254–260.
- (48) Feng, X.; Xie, C.; Liu, Z.; Xie, Y.; King, R. B.; Schaefer Iii, H. F. *Dalton Trans.* **2009**, 2599–2608.
- (49) Bylaska, E. J.; Jong, W. A. d.; Govind, N.; Kowalski, K.; Straatsma, T. P.; Valiev, M.; Wang, D.; Apra, E.; Windus, T. L.; Hammond, J.; Nichols, P.; Hirata, S.; Hackler, M. T.; Zhao, Y.; Fan, P.-D.; Harrison, R. J.; Dupuis, M.; Smith, D. M. A.; Nieplocha, J.; Tipparaju, V.; Krishnan, M.; Wu, Q.; Voorhis, T. V.; Auer, A. A.; Nooijen, M.; Brown, E.; Cisneros, G.; Fann, G. I.; Fruchtl, H.; Garza, J.; Hirao, K.; Kendall, R.; Nichols, J. A.; Tsemekhman, K.; Wolinski, K.; Anchell, J.; Bernholdt, D.; Borowski, P.; Clark, T.; Clerc, D.; Dachsels, H.; Deegan, M.; Dyall, K.; Elwood, D.; Glending, E.; Gutowski, M.; Hess, A.; Jaffe, J.; Johnson, B.; Ju, J.; Kobayashi, R.; Kutteh, R.; Lin, Z.; Littlefield, R.; Long, X.; Meng, B.; Nakajima, T.; Niu, S.; Pollack, L.; Rosing, M.; Sandrone, G.; Stave, M.; Taylor, H.; Thomas, G.; Lenthe, J. v.; Wong, A.; Zhang, Z. *NWChem, A Computational Chemistry Package for Parallel Computers*, 5.1; Pacific Northwest National Laboratory: Richland, WA 99352–0999, USA, 2007.
- (50) Frisch, M. J.; Trucks, G. W.; Schlegel, H. B.; Scuseria, G. E.; Robb, M. A.; Cheeseman, J. R.; Montgomery, J. A., Jr.; Vreven, T.; Kudin, K. N.; Burant, J. C.; Millam, J. M.; Iyengar, S. S.; Tomasi, J.; Barone, V.; Mennucci, B.; Cossi, M.; Scalmani, G.; Rega, N.; Petersson, G. A.; Nakatsuji, H.; Hada, M.; Ehara, M.; Toyota, K.; Fukuda, R.; Hasegawa, J.; Ishida, M.; Nakajima, T.; Honda, Y.; Kitao, O.; Nakai, H.; Klene, M.; Li, X.; Knox, J. E.; Hratchian, H. P.; Cross, J. B.; Adamo, C.; Jaramillo, J.; Gomperts, R.; Stratmann, R. E.; Yazyev, O.; Austin, A. J.; Cammi, R.; Pomelli, C.; Ochterski, J. W.; Ayala, P. Y.; Morokuma, K.; Voth, G. A.; Salvador, P.; Dannenberg, J. J.; Zakrzewski, V. G.; Dapprich, S.; Daniels, A. D.; Strain, M. C.;

Farkas, O.; Malick, D. K.; Rabuck, A. D.; Raghavachari, K.; Foresman, J. B.; Ortiz, J. V.; Cui, Q.; Baboul, A. G.; Clifford, S.; Cioslowski, J.; Stefanov, B. B.; Liu, G.; Liashenko, A.; Piskorz, P.; Komaromi, I.; Martin, R. L.; Fox, D. J.; Keith, T.; Al-Laham, M. A.; Peng, C. Y.; Nanayakkara, A.; Challacombe, M.; Gill, P. M. W.; Johnson, B.; Chen, W.; Wong, M. W.; Gonzalez, C.; Pople, J. A. *GAUSSIAN 03*; Gaussian Inc.: Pittsburgh, PA, 2003.

- (51) Becke, A. D. *J. Chem. Phys.* **1993**, *98*, 5648.
- (52) Lee, C.; Yang, W.; Parr, R. G. *Phys. Rev. B* **1988**, *37*, 785.
- (53) Cundari, T. R.; Stevens, W. J. *J. Chem. Phys.* **1993**, *98*, 5555.
- (54) Stevens, W.; Basch, H.; Krauss, J. *J. Chem. Phys.* **1984**, *81*, 6026.
- (55) Stevens, W. J.; Krauss, M.; Basch, H.; Jasien, P. G. *Can. J. Chem.* **1992**, *70*, 612.
- (56) Woon, D. E.; Dunning, T. H., Jr. *J. Chem. Phys.* **1993**, *98*, 1358.
- (57) Wilson, A.; van Mourik, T.; Dunning, T. H., Jr. *J. Mol. Struct.* **1997**, *388*, 339.
- (58) Peterson, K. A.; Woon, D. E.; Dunning, T. H., Jr. *J. Chem. Phys.* **1994**, *100*, 7410.
- (59) Kendall, R. A., Jr.; T., H. D.; Harrison, R. J. *J. Chem. Phys.* **1992**, *96*, 6796.
- (60) Dunning, T. H., Jr. *J. Chem. Phys.* **1989**, *90*, 1007.
- (61) Boys, S. F.; Bernardi, F. *Mol. Phys.* **1970**, *19*, 553.
- (62) Ochterski, J. W. *Thermochemistry in Gaussian*; Gaussian, Inc.: Pittsburgh, PA, 2000; pp 1–19.
- (63) Hieber, W.; Lagally, H. *Z. Anorg. Allg. Chem.* **1943**, *251*, 96–113.
- (64) Giuffrida, S.; Barone, G.; Duca, D. *J. Chem. Inf. Model.* **2009**, *49*, 1223–1233.
- (65) Mojet, B. L.; Koningsberger, D. C. *Catal. Lett.* **1996**, *39*, 191–196.
- (66) Knickelbein, M. B. *J. Chem. Phys.* **2002**, *116*, 9703.
- (67) Castner, D. G.; Sexton, B. A.; Somorjai, G. A. *Surf. Sci.* **1978**, *71*, 519–540.
- (68) Singh, H. P. *Acta Crystallogr. A* **1968**, *24*, 469.
- (69) McHale, J. L. *Molecular Spectroscopy*; Prentice Hall: Upper Saddle River, NJ, 1999.
- (70) Severson, M. W.; Stuhlmann, C.; Villegas, I.; Weaver, M. J. *J. Chem. Phys.* **1995**, *103*, 9832–9843.
- (71) Persson, B. N. J.; Ryberg, R. *Phys. Rev. B* **1981**, *24*, 6954–6970.
- (72) Atkins, P. W.; Friedman, R. S. *Molecular Quantum Mechanics*, 3rd ed.; Oxford University Press: Oxford, U.K., 1997.
- (73) Zeinalipour-Yazdi, C. D.; Pullman, D. P. *J. Phys. Chem. B* **2008**, *112*, 7377–7386.
- (74) Zeinalipour-Yazdi, C. D.; Pullman, D. P. *J. Phys. Chem. B* **2009**, *113*, 9628.
- (75) Zeinalipour-Yazdi, C. D.; Pullman, D. P. *J. Phys. Chem. B* **2006**, *110*, 24260–24265.